Research Square

Preprints are preliminary reports that have not undergone peer review.
They should not be considered conclusive, used to inform clinical practice,
or referenced by the media as validated information.

Virtual Contact Loop: Performance-Oriented Cartesian Impedance Synthesis for Robotic Manipulators

Changjun Li
Department of Mechanical Engineering, Xi'an Jiaotong University
Fei Zhao
ztzhao@mail.xjtu.edu.cn
[illegible]
Tao Tao
[illegible]
Xuesong Mei
[illegible]
Hu Shi
[illegible]

Research Article

Keywords: Cartesian impedance control, virtual contact loop, performance-oriented impedance synthesis, coupled MIMO systems, $\mathcal H_2/\mathcal H_\infty$ performance, time-varying impedance, Lyapunov stability

Posted Date: November 9th, 2026

DOI: https://doi.org/10.21203/rs.3.rs-11639508/v1

License: This work is licensed under a Creative Commons Attribution 4.0 International License.
Read Full License

Additional Declarations: The authors declare no competing interests.

Virtual Contact Loop: Performance-Oriented Cartesian Impedance Synthesis for Robotic Manipulators

Changjun Li, Fei Zhao*, Tao Tao, Xuesong Mei, and Hu Shi

***Abstract*—Cartesian impedance control is widely used to regulate physical interaction between robots and their environments. However, the configuration-dependent inertia and strong coupling of Cartesian dynamics make the systematic design of damping and stiffness matrices challenging. This paper proposes a performance-oriented Cartesian impedance synthesis method based on a virtual contact loop, termed VCL-IS. The virtual loop tracks the theoretical response of a desired impedance over a prescribed frequency range, converting impedance design into a weighted generalized-plant optimization problem. The synthesis objective combines weighted $\mathcal{H}_2$ and $\mathcal{H}_\infty$ performance with the negative spectral abscissa to balance compliance, aggregate robustness, and asymptotic convergence. Two- and six-dimensional simulations demonstrate that VCL-IS exploits dynamic coupling to achieve larger compliant displacements with low overshoot at comparable response speeds. The optimized damping and stiffness matrices exhibit interpretable modal relationships with the target bandwidth. For configuration-dependent inertia, a common quadratic Lyapunov analysis yields a sufficient admissible interval for time-varying modal frequencies, which is enforced in an SAC-based adaptation policy. Physical-robot experiments further show closer agreement between theoretical and measured six-dimensional responses than the baseline methods. These results support VCL-IS as an interpretable framework for performance-oriented synthesis and time-varying extension of coupled Cartesian impedance.**

***Index Terms*—Cartesian impedance control, virtual contact loop, performance-oriented impedance synthesis, coupled MIMO systems, $\mathcal{H}_2/\mathcal{H}_\infty$ performance, time-varying impedance, Lyapunov stability.**

I. Introduction

Impedance control regulates physical interaction between a robot and its environment by shaping the dynamic relationship between end-effector interaction forces and motion deviations. It enables a robot to exhibit prescribed mechanical behavior during contact with uncertain environments [1]–[3]. Research on Cartesian stiffness control, compliant motion, and hybrid force/position control has established important foundations for physical robot–environment interaction [2], [3]. Operational-space dynamics further provide a systematic description of end-effector motion and interaction forces, while revealing the dependence of Cartesian inertia on robot configuration and the Jacobian matrix [4], [5].

Department of Mechanical Engineering, Xi'an Jiaotong University, Xi'an 710049, China.

State Key Laboratory for Manufacturing Systems Engineering, Xi'an Jiaotong University, Xi'an 710054, China.

* E-mail: ztzhao@mail.xjtu.edu.cn.

Despite its broad use, Cartesian impedance parameterization remains challenging. The Cartesian dynamics of a robot constitute a configuration-dependent, strongly coupled MIMO system. The desired impedance model is defined as follows:

$$\begin{aligned} \boldsymbol{F}_{\text{ext}}(t) &= \boldsymbol{\Lambda}_d \Delta\ddot{\boldsymbol{x}}(t) + \boldsymbol{D}_d \Delta\dot{\boldsymbol{x}}(t) + \boldsymbol{K}_d \Delta\boldsymbol{x}(t), \\ \boldsymbol{F}_{\text{ext}}(s) &= \boldsymbol{Z}(s)\Delta\boldsymbol{x}(s), \\ \boldsymbol{Z}(s) &= \boldsymbol{\Lambda}_d s^2 + \boldsymbol{D}_d s + \boldsymbol{K}_d. \end{aligned} \tag{1}$$

Here, $\boldsymbol{\Lambda}_d$, $\boldsymbol{D}_d$, and $\boldsymbol{K}_d$ denote the desired inertia, damping, and stiffness matrices, respectively, and $\Delta\boldsymbol{x}$ is the equilibrium displacement induced by the external force $\boldsymbol{F}_{\text{ext}}$. For controller simplification, the desired Cartesian inertia is often selected to match the actual Cartesian inertia. The inertia matrix is symmetric positive definite, and its off-diagonal entries represent dynamic coupling among translational and rotational degrees of freedom. Consequently, an external force applied along one Cartesian direction may induce motion in several directions, while the response along that direction may also be affected by impedance parameters in other directions. The matrices $\boldsymbol{\Lambda}_d$, $\boldsymbol{D}_d$, and $\boldsymbol{K}_d$ should therefore be designed as complete symmetric positive-definite matrices rather than by independently tuning multiple single-input–single-output (SISO) channels [4]–[7].

Conventional impedance-design methods generally prescribe modal frequencies and damping ratios in advance. Such parameterizations do not directly express task-level, multidimensional interaction objectives. In practical interaction tasks, impedance design must balance compliance, transient response, convergence speed, and robustness against external disturbances, model errors, and parameter variations. These properties are mutually coupled, and no single performance measure is sufficient to characterize the overall interaction behavior.

To address this issue, this paper proposes a virtual-contact-loop-based impedance synthesis method, termed VCL-IS. The method constructs a virtual feedback loop that tracks the theoretical response trajectory of a candidate impedance under an external contact force. By selecting the virtual-loop bandwidth appropriately, the virtual closed-loop response approximates the desired impedance response over a prescribed frequency range. This establishes a mapping between impedance parameters and a virtual control system, transforming impedance design into a performance-optimization problem for a weighted generalized plant. The weighted $\mathcal{H}_2/\mathcal{H}_\infty$ performance is used to evaluate and optimize compliance and aggregate robust-

ness, whereas the negative spectral abscissa characterizes the asymptotic convergence rate. Their combination provides a unified framework for balancing compliance, convergence, and aggregate robustness.

The Cartesian inertia of a robot varies with its configuration, so impedance synthesis must also be extended to time-varying systems. Time-varying damping and stiffness introduce additional stability issues: stability of each frozen-time impedance model does not by itself guarantee stability of the overall time-varying system [8]–[12]. Based on the structured damping and stiffness spectra identified in the fixed-inertia synthesis, this paper develops a time-varying impedance parameterization and derives a sufficient modal-frequency constraint using a common quadratic Lyapunov function. The constraint is incorporated into a Soft Actor–Critic (SAC) policy to generate time-varying impedance parameters while respecting the derived stability bound [9], [13]–[18].

The main contributions are summarized as follows:

1) A coupled Cartesian impedance synthesis method based on a virtual contact loop is proposed. The mapping between candidate impedance parameters and the virtual closed-loop system provides a unified framework for performance-oriented design of coupled MIMO systems.
2) An interaction-performance evaluation and optimization criterion is established. The weighted $\mathcal{H}_2/\mathcal{H}_\infty$ performance of the generalized plant and the negative spectral abscissa are combined to balance compliance, asymptotic convergence, and aggregate robustness.
3) The empirical structure of the optimized impedance matrices is analyzed using two- and six-dimensional coupled-system simulations. Directional trends of the damping and stiffness spectra with respect to the design bandwidth are identified.
4) A time-varying extension is developed. A common quadratic Lyapunov function yields a sufficient admissible range for the modal frequencies, which is imposed on an SAC policy. The practical impedance realization is evaluated on a seven-degree-of-freedom robot.

II. Related Work

Impedance control shapes physical interaction between a robot and its environment by defining the dynamic relationship between interaction force and motion response [1]. Early studies on Cartesian stiffness control, compliant motion, and force control established the foundations of robot contact interaction [2], [3]. Operational-space dynamics subsequently provided a unified description of end-effector motion and force [4], [5]. For coupled MIMO systems, previous research has considered matrix impedance parameterization, dynamic decoupling, passivity, and robot–environment interaction stability [6], [7], [19], [20]. Nevertheless, determining impedance matrices that achieve a suitable balance among compliance, convergence, and aggregate robustness remains an important design problem.

Several approaches have been proposed to construct coupled Cartesian damping and stiffness matrices. Factorized coupled impedance configuration (FAC) uses inertia-matrix factorization and prescribed modal parameters to construct coupled damping and stiffness matrices. The double-diagonalization (DD) approach employs a different matrix expression for damping while retaining a structured stiffness parameterization. These methods can produce symmetric matrices with nonzero off-diagonal entries, but their parameters are still primarily determined by prescribed modal frequencies and damping ratios [6], [19]. Saldarriaga et al. analytically selected Cartesian damping-matrix elements through joint-space vibration analysis to suppress selected vibration modes while preserving the desired Cartesian dynamic response [21]. For redundant robots performing constrained tasks, Lachner et al. shaped task impedances according to time-varying inertial properties and virtual constraints, with a damping design that preserves passivity and the desired task-space behavior [33]. Cartesian diagonal impedance (DCI) and diagonalized Cartesian impedance (dDCI) are used as diagonal baselines, with diagonal parameters assigned in the Cartesian frame and an inertia-related coordinate frame, respectively. Related work on Cartesian impedance and operational-space parameterization provides the theoretical background for these baselines [4], [6], [7], [19]. Although straightforward to implement, predefined coordinate directions or transformed diagonal parameterizations may not fully exploit the design freedom of a generally coupled impedance matrix.

From the viewpoint of control-system performance, the $\mathcal{H}_2$ and $\mathcal{H}_\infty$ norms provide complementary measures of energy-related response and worst-case input–output gain, respectively. Generalized plants and weighting functions can be used to describe multiple performance channels in a unified manner. Related studies have applied robust control, linear matrix inequalities (LMIs), and μ-synthesis to robot impedance and interaction control; these studies and standard multivariable robust-control references provide the relevant background [22]–[28]. In this paper, additive impedance-parameter mismatch is represented as an equivalent disturbance input. The perturbed and nominal impedance equations are written as follows:

$$\begin{aligned}&(\boldsymbol{\Lambda}_d+\Delta\boldsymbol{\Lambda})\Delta\ddot{\boldsymbol{x}}+(\boldsymbol{D}_d+\Delta\boldsymbol{D})\Delta\dot{\boldsymbol{x}}\\&\quad+(\boldsymbol{K}_d+\Delta\boldsymbol{K})\Delta\boldsymbol{x}=\boldsymbol{F}_{\text{ext}}+\boldsymbol{F}_{\text{dis}},\\&\boldsymbol{\Lambda}_d\Delta\ddot{\boldsymbol{x}}+\boldsymbol{D}_d\Delta\dot{\boldsymbol{x}}+\boldsymbol{K}_d\Delta\boldsymbol{x}=\boldsymbol{F}_{\text{ext}}+\boldsymbol{F}_{\text{dis}}-\boldsymbol{F}_\Delta=\boldsymbol{F}_{\text{ext}}+\boldsymbol{F}_{\text{dis}}^{+}.\end{aligned}\tag{2}$$

The equivalent force mismatch is defined as follows:

$$\boldsymbol{F}_\Delta=\Delta\boldsymbol{\Lambda}\Delta\ddot{\boldsymbol{x}}+\Delta\boldsymbol{D}\Delta\dot{\boldsymbol{x}}+\Delta\boldsymbol{K}\Delta\boldsymbol{x},\qquad\boldsymbol{F}_{\text{dis}}^{+}=\boldsymbol{F}_{\text{dis}}-\boldsymbol{F}_\Delta.$$

Thus, external disturbances and impedance-parameter mismatch can be incorporated into a common disturbance channel. Their attenuation is referred to as *aggregate robustness* throughout this paper. This definition does not distinguish the individual contribution of each uncertainty or disturbance source.

The asymptotic convergence rate is another important consideration in impedance design. For a continuous-time state-space system, the spectral abscissa is the largest real part among the eigenvalues of its state matrix. Its negative is defined here as the negative spectral abscissa:

$$\alpha=-\max_i\operatorname{Re}[\lambda_i(\boldsymbol{A}_d)]\,.\tag{3}$$

Here, $\boldsymbol{A}_d$ is the state matrix of the desired impedance system. The system is asymptotically stable if $\alpha > 0$, and a larger α indicates a faster asymptotic exponential convergence rate under otherwise comparable conditions. However, eigenvalue locations alone cannot fully characterize transient amplification in non-normal systems or sensitivity to parameter perturbations. These limitations have been discussed in studies of eigenvalue optimization and pseudospectral analysis [29], [30]. Therefore, α is used as an indicator of asymptotic convergence rather than as a complete transient-performance metric or a proof of robust stability.

The time variation of the Cartesian inertia matrix $\boldsymbol{\Lambda}$ and task uncertainty motivate real-time impedance adaptation. However, parameter variation affects system energy and stability, and frozen-time stability does not guarantee stability of the complete time-varying system [8]. Energy-tank methods constrain energy exchange between the robot and its environment to preserve passivity [31], [32]. Other studies have derived stability conditions for time-varying impedance using model-based and passivity-based analyses, including extensions to redundant manipulators and variable-compliance control [8]–[12]. Learning-based methods have also been investigated for variable-impedance generation and adaptation, including learning from demonstrations, interaction experience, and reinforcement learning [9], [13]–[16]. For contact-rich manipulation, Zhou et al. learned a variable-impedance policy from human demonstrations using RGB-D and force/torque observations [34]. Tang et al. combined an adaptive impedance controller with a multi-source-feedback DDPG stiffness controller in a parallel electromagnetic variable-stiffness manipulator for compliant grinding [35]. SAC supports off-policy learning in continuous action spaces and is therefore suitable for continuous impedance-parameter generation [17], [18]. Nevertheless, optimizing instantaneous task performance alone does not guarantee stability of the overall time-varying impedance system; an explicit stability constraint is required.

In summary, previous studies have advanced robot impedance control through coupled-matrix construction, robust-performance evaluation, time-varying stability analysis, and learning-based adaptation. This paper addresses the lack of a unified impedance-synthesis framework that combines weighted input–output performance with asymptotic convergence. VCL-IS establishes the required mapping through a virtual contact loop and uses the weighted $\mathcal{H}_2/\mathcal{H}_\infty$ performance and negative spectral abscissa for performance-oriented synthesis. The empirical impedance structure is then used to construct a time-varying parameterization, while a common-quadratic-Lyapunov sufficient condition constrains the modal bandwidth generated by SAC.

III. Virtual-Contact-Loop-Based Impedance Synthesis

The design of a desired impedance is a primary problem in robot–environment interaction. Conventional parameterization methods focus mainly on impedance modes, whereas interaction-oriented design must jointly consider compliance, dynamic convergence, and aggregate robustness. Direct optimization is difficult for strongly coupled MIMO systems because these properties interact in a nontrivial manner. Nevertheless, their effects are ultimately reflected in the resulting robot–environment interaction. The central idea of VCL-IS is therefore to construct a virtual contact loop and infer impedance parameters from the desired interaction performance.

A. Virtual Contact Loop and Impedance Mapping

Let $\Delta\boldsymbol{x}$ denote the desired impedance response under the contact force $\boldsymbol{F}_{\text{ext}}$. VCL-IS constructs a virtual feedback controller whose objective is to realize this response. The virtual contact loop consists of a virtual controller $\boldsymbol{C}(s)$, a virtual plant $\boldsymbol{P}(s)$, and a unity negative-feedback connection. The virtual closed-loop response is denoted by $\Delta\boldsymbol{x}_r$. When the output of $\boldsymbol{C}(s)$ is interpreted as the contact force, a deterministic mapping exists between the virtual loop and the impedance model, as illustrated in Fig. 1.

The virtual closed-loop response is not required to be identical to the ideal impedance response at all frequencies. Instead, the open-loop transfer function is designed so that the closed-loop tracking behavior is prescribed. In this work, the first-order Butterworth low-pass response is defined as follows:

$$\begin{aligned} \Delta\boldsymbol{x}_r(s) &= \boldsymbol{H}(s)\Delta\boldsymbol{x}(s), \\ \boldsymbol{H}(s) &= \frac{\omega_c}{s+\omega_c}\boldsymbol{I}. \end{aligned} \tag{4}$$

Here, ω_c is the -3 dB cutoff angular frequency of $\boldsymbol{H}(s)$. Combining (1) and (4) with the loop structure gives the following virtual controller and plant:

$$\begin{aligned} \boldsymbol{C}(s) &= \frac{s+\omega_c}{s}\boldsymbol{Z}(s), \\ \boldsymbol{P}(s) &= \frac{\omega_c}{s+\omega_c}\boldsymbol{Z}^{-1}(s). \end{aligned} \tag{5}$$

Thus, once $\boldsymbol{H}(s)$ (or equivalently ω_c) is specified, the virtual contact loop is completely determined by the candidate impedance $\boldsymbol{Z}(s)$.

The impedance-performance analysis can consequently be converted into an analysis of the virtual contact loop. The frequency range used for virtual-loop approximation and impedance-performance evaluation is $\omega \in [0, \omega_b]$, where ω_b is the target design bandwidth. To make the virtual response sufficiently close to the desired impedance response over this range, the theoretical requirement is $\omega_c > 11.43\,\omega_b$. At $\omega_c = 11.43\omega_b$, the magnitude attenuation of $\Delta\boldsymbol{x}_r$ relative to $\Delta\boldsymbol{x}$ at ω_b is approximately 0.381%, the phase lag is approximately 5.00°, and the sinusoidal steady-state tracking error is approximately 8.72%. At $\omega_c = 20\omega_b$, the corresponding values are approximately 0.125%, 2.86°, and 4.99%, respectively; this ratio is therefore adopted in all numerical simulations and physical experiments reported in this paper. Increasing the ratio ω_c/ω_b improves tracking accuracy within the design range. Under this condition, the response characteristics of $\Delta\boldsymbol{x}$ can be approximated by those of $\Delta\boldsymbol{x}_r$ for performance evaluation.

The virtual controller $\boldsymbol{C}(s)$ and virtual plant $\boldsymbol{P}(s)$ are functions of the candidate impedance matrix $\boldsymbol{Z}(s)$ once ω_b and ω_c are selected. The virtual contact loop is not an

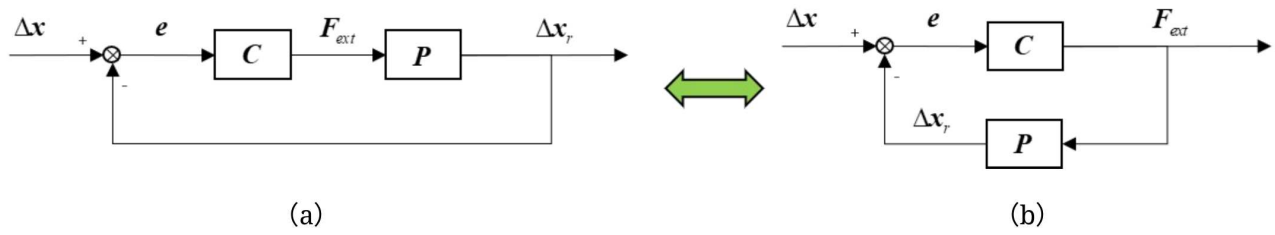


Fig. 1. Virtual contact loop used to map impedance characteristics to closed-loop performance. (a) Virtual feedback loop, illustrating the ability of the virtual controller to realize the desired response. (b) Equivalent mapping between the virtual contact loop and the impedance model.

additional physical controller to be deployed on the robot; it is an analytical construction used to evaluate and synthesize candidate impedance matrices.

B. Performance-Oriented Impedance Synthesis

VCL-IS jointly considers compliance, dynamic convergence, and aggregate robustness. The asymptotic convergence rate is characterized by α in (3). The virtual-loop dynamic response, determined by the design parameters ω_b and ω_c, is used to characterize the impedance response.

Several closed-loop sensitivity functions are fixed by the selected virtual-loop structure:

$$\begin{aligned} \boldsymbol{T}(s) &= \boldsymbol{H}(s) = \frac{\omega_c}{s+\omega_c}\boldsymbol{I}, \\ \boldsymbol{S}_i(s) &= \boldsymbol{I} - \boldsymbol{H}(s) = \frac{s}{s+\omega_c}\boldsymbol{I}, \\ \boldsymbol{S}_u(s) &= -[\boldsymbol{I} + \boldsymbol{C}(s)\boldsymbol{P}(s)]^{-1}\boldsymbol{C}(s)\boldsymbol{P}(s) = -\frac{\omega_c}{s+\omega_c}\boldsymbol{I}. \end{aligned} \tag{6}$$

However, the sensitivity from the equivalent disturbance to the disturbance-induced response is directly related to the admittance $\boldsymbol{Z}^{-1}(s)$:

$$\boldsymbol{S}(s) = [\boldsymbol{I} + \boldsymbol{P}(s)\boldsymbol{C}(s)]^{-1}\boldsymbol{P}(s) = \frac{\omega_c s}{(s+\omega_c)^2}\boldsymbol{Z}^{-1}(s). \tag{7}$$

When the equivalent disturbance is considered, the force balance in the loop can be expressed as

$$\boldsymbol{F}_{\text{ext}}(s) = \boldsymbol{Z}(s)\Delta\boldsymbol{x}(s) - \boldsymbol{H}(s)\boldsymbol{F}^{+}_{\text{dis}}(s). \tag{8}$$

The second term in (8) reflects the coupling between impedance compliance and disturbance/parameter mismatch, whereas $\boldsymbol{S}(s)$ characterizes the aggregate disturbance response of the loop.

To evaluate compliance and aggregate robustness in a unified framework, weighting functions $\boldsymbol{W}_u(s)$ and $\boldsymbol{W}_d(s)$ are assigned to the two performance channels. The resulting generalized plant is given by:

$$\boldsymbol{G}_{\text{VLC}}(s) = \begin{bmatrix} \boldsymbol{W}_u(s)\boldsymbol{Z}(s) & -\boldsymbol{W}_u(s)\boldsymbol{H}(s) \\ \boldsymbol{0} & \boldsymbol{W}_d(s)\boldsymbol{S}(s) \end{bmatrix}. \tag{9}$$

The input is $\boldsymbol{w}(s) = [\Delta\boldsymbol{x}^T(s), (\boldsymbol{F}^{+}_{\text{dis}}(s))^T]^T$. The two output channels represent the weighted contact force required to realize the desired response and the weighted disturbance-induced response, respectively. To maintain high compliance while improving aggregate robustness, both outputs should be minimized. According to robust-control theory, the $\mathcal{H}_2$ and $\mathcal{H}_\infty$ norms of the generalized plant quantify energy-related and worst-case input–output gains, respectively. Combining these measures with the asymptotic convergence rate α, the impedance-performance loss is defined as follows:

$$\begin{aligned} L &= \frac{\gamma}{\ln(1+e^{\alpha})}, \\ \gamma &= \|\boldsymbol{G}_{\text{VLC}}(s)\|_2 + \|\boldsymbol{G}_{\text{VLC}}(s)\|_\infty . \end{aligned} \tag{10}$$

The loss function in (10) is not unique; it is one scalarization that encourages a reduction in the $\mathcal{H}_2/\mathcal{H}_\infty$ norms of the generalized plant while increasing α. For fixed $\boldsymbol{\Lambda}_d$, ω_b, ω_c, and weighting functions, the desired damping and stiffness matrices are obtained by solving the following constrained optimization problem:

$$\begin{aligned} (\boldsymbol{D}_{d,\text{opt}}, \boldsymbol{K}_{d,\text{opt}}) &\in \arg\min_{\boldsymbol{D}_d, \boldsymbol{K}_d} L(\boldsymbol{D}_d, \boldsymbol{K}_d), \\ \text{subject to} \quad & \boldsymbol{D}_d = \boldsymbol{D}_d^T \succ \boldsymbol{0}, \qquad \boldsymbol{K}_d = \boldsymbol{K}_d^T \succ \boldsymbol{0}. \end{aligned}$$

Here, the subscript opt identifies a minimizing pair of desired damping and stiffness matrices.

IV. VCL-IS Synthesis Examples and Empirical Mechanism

This section evaluates the VCL-IS synthesis results and examines the structure of the optimized impedance matrices using selected weighting functions and numerical simulations.

A. Selection of Weighting Functions

The generalized plant in (9) contains two performance channels. The weighting functions $\boldsymbol{W}_u(s)$ and $\boldsymbol{W}_d(s)$ determine the relative importance of compliance and aggregate robustness. The compliance channel is affected by both the desired response and the equivalent disturbance; therefore, $\boldsymbol{W}_u(s)$ is selected as a low-pass or band-pass filter. The aggregate-robustness channel is driven by the equivalent disturbance, so $\boldsymbol{W}_d(s)$ can be selected as a band-pass or high-pass filter. In this study, a third-order Butterworth low-pass filter and a second-order Butterworth high-pass filter are used:

$$\begin{aligned} \boldsymbol{W}_u(s) &= \frac{G_u\omega_b^3}{s^3 + 2\omega_b s^2 + 2\omega_b^2 s + \omega_b^3}\boldsymbol{I}, \\ \boldsymbol{W}_d(s) &= \frac{G_d s^2}{s^2 + \sqrt{2}\omega_b s + \omega_b^2}\boldsymbol{I}. \end{aligned} \tag{11}$$

Minimizing the weighted compliance-channel output favors a large response to low-frequency contact forces, corresponding

to high compliance. Minimizing the weighted disturbance-channel output suppresses the response to equivalent disturbances, corresponding to improved aggregate robustness. Since $\boldsymbol{Z}(s)$ is a second-order transfer matrix, a third-order or higher-order low-pass filter is required in the compliance channel to ensure sufficient high-frequency attenuation. A second-order or lower-order low-pass filter may otherwise leave a nonzero high-frequency contribution through the product involving $\boldsymbol{H}(s)$. The weighting gains G_u and G_d are key design parameters; their ratio

$$\rho = \frac{G_u}{G_d}$$

determines the relative emphasis placed on compliance and aggregate robustness.

B. Optimization Results for Two- and Six-Dimensional Systems

VCL-IS is applied to two-dimensional and six-dimensional inertia matrices. The two-dimensional system facilitates visualization and is used for orthogonal tests of the inertia matrix and target bandwidth. The six-dimensional system provides a more demanding test of strong coupling. The weighting ratio is set to $\rho = 1$, consistent with the experimental setting.

For the two-dimensional tests, four different desired inertia matrices $\boldsymbol{\Lambda}_d$ are considered, and the target bandwidth ω_b is independently set to 15, 20, and 25 rad/s. For each given inertia matrix and target bandwidth, a search algorithm is used to find $\boldsymbol{D}_d$ and $\boldsymbol{K}_d$ that minimize L. The same step contact force is applied to every candidate impedance. The force is applied at approximately 0.3 s and removed at 1.8 s, along the centerline direction of the X–Y plane. The dDCI, DCI, FAC, DD, and VCL-IS methods are compared under each condition. The damping and stiffness matrices are constrained to be symmetric positive definite for all methods. The results are shown in Fig. 2.

The simulations reveal a consistent performance trade-off. Under the tested conditions, dDCI and DCI tend to produce larger compliant displacements, but provide the weakest overshoot suppression and exhibit greater sensitivity to the inertia representation. Diagonal parameterization may either suppress or amplify coupling effects; therefore, the overall response cannot be inferred from diagonal parameters alone. FAC and DD generally produce faster responses and smaller overshoots, but their smaller steady-state displacements indicate lower compliance. For some inertia matrices, the compliance and overshoot behavior of FAC and DD changes noticeably, suggesting sensitivity to the selected inertia representation. In contrast, VCL-IS maintains relatively fast responses, smooth transients, and very small overshoots while producing larger equilibrium displacements across the tested conditions. In several cases, the FAC and DD response curves are close to one another; this observation applies only to the tested matrices and parameter settings and should not be interpreted as general equivalence between the two methods. Since the desired response speed increases with the target bandwidth, all tested methods exhibit a reduction in compliance as the target response becomes faster.

The six-dimensional $\boldsymbol{\Lambda}_d$ synthesis test evaluates the methods on a strongly coupled Cartesian inertia matrix extracted from a representative robot configuration. The normalized inertia matrix contains substantial off-diagonal terms, as shown in Fig. 3. For example, the normalized coupling coefficients between R_y and P_x, between R_x and P_y, and between R_x and R_z are 0.91, −0.85, and 0.77, respectively. These values indicate pronounced coupling rather than an approximately diagonal structure.

The same contact-force profile as in the two-dimensional tests is applied along the centerline of the x–y plane, with application and removal times of 0.3 and 1.8 s, respectively. The six-dimensional response projections, rotational and translational response measures, and individual Cartesian-axis responses are compared in Fig. 4. In this test, dDCI does not produce a valid and stable rotational response, potentially because its diagonal parameterization is not suitable for the cross-dimensional and cross-scale coupling between the three rotational and three translational axes. DCI exhibits a pronounced unstable tendency in the rotational response, consistent with its neglect of inertia coupling. FAC and DD produce similar responses. Compared with these two methods, VCL-IS produces larger compliant responses with a comparable settling time and nearly eliminates overshoot.

The six-dimensional displacement measure combines rotational and translational deviations using a characteristic length of 0.1 m:

$$\|\Delta x\| = \sqrt{0.1^2\|\Delta\theta\|_2^2 + \|\Delta p\|_2^2}.$$

Here, $\Delta\theta$ and Δp denote the rotational and translational displacement deviations, respectively.

The quantitative response measures are summarized in Table I. Rotational and translational response norms are reported separately because their units differ.

For the reported six-dimensional test, the VCL-IS rotational peak norm increases from 0.2484 rad for FAC/DD to 0.3231 rad, while the translational peak norm increases from 0.0330 m to 0.0433 m, indicating higher compliance. The VCL-IS settling time is approximately 0.482–0.484 s, slightly longer than the 0.423 s obtained with FAC/DD, but its overshoot is nearly eliminated. Its residual error is small, although it is not the smallest among all methods. Thus, VCL-IS does not dominate every individual metric; rather, it provides a favorable balance between compliance and transient response under the tested conditions.

C. Empirical Structure of the Optimized Impedance

The optimized impedance matrices exhibit a geometrically interpretable structure. Since the Cartesian inertia matrix is symmetric positive definite, it can be represented geometrically by an inertia ellipsoid. Its eigendecomposition is given by:

$$\boldsymbol{\Lambda}_d = \boldsymbol{V}\boldsymbol{\lambda}_\Lambda\boldsymbol{V}^T.$$

Here, $\boldsymbol{V}$ contains the eigenvectors and defines the orientation of the ellipsoid, while the diagonal entries of $\boldsymbol{\lambda}_\Lambda$ determine its principal-axis scales. In VCL-IS, impedance decoupling is achieved through pose matching: the damping and stiffness

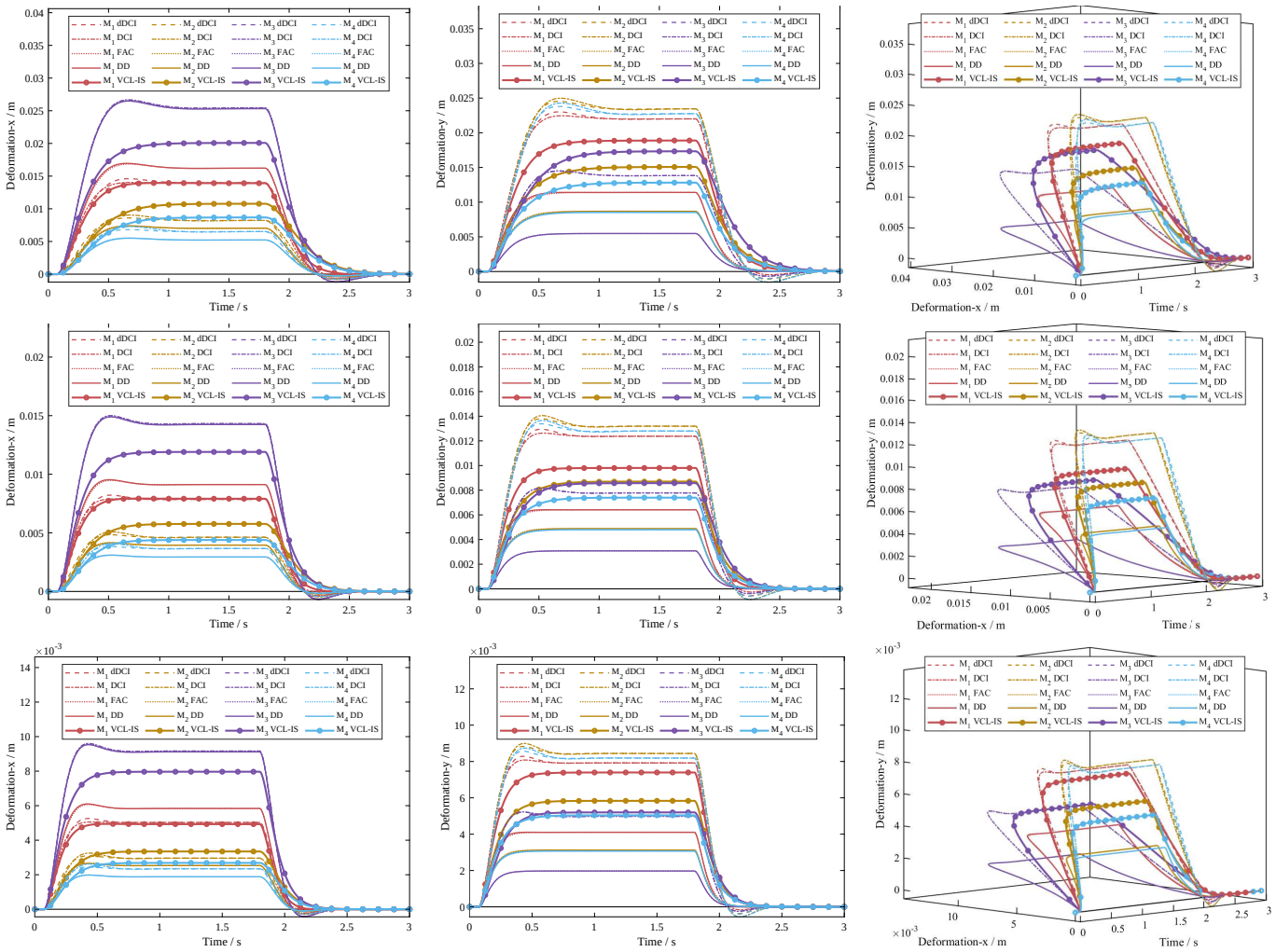


Fig. 2. Two-dimensional step responses for four desired inertia matrices $\mathbf{\Lambda}_d$ and three target design bandwidths ω_b. From top to bottom, the rows correspond to target bandwidths of 15, 20, and 25 rad/s. The columns show the x-direction response, the y-direction response, and the time evolution of the two-dimensional response trajectory in the x–y plane, respectively.

TABLE I
SIX-DIMENSIONAL CARTESIAN IMPEDANCE RESPONSE METRICS.

Method	Response measure	Peak magnitude	Settling time (s)	Overshoot (%)	Return time (s)	Residual error
dDCI	Rotational norm (rad)	—	—	—	—	—
dDCI	Translational norm (m)	1.3116×10^{-2}	0.810	4.6788	0.799	2.6349×10^{-5} m
DCI	Rotational norm (rad)	2.2611×10^{-2}	—	1577	—	4.7297×10^{-3} rad
DCI	Translational norm (m)	1.3600×10^{-2}	1.297	9.3198	—	3.5156×10^{-4} m
FAC	Rotational norm (rad)	2.4839×10^{-1}	0.423	4.5989	0.421	7.4717×10^{-7} rad
FAC	Translational norm (m)	3.3043×10^{-2}	0.423	4.5989	0.421	9.9393×10^{-8} m
DD	Rotational norm (rad)	2.4839×10^{-1}	0.423	4.5989	0.421	7.4717×10^{-7} rad
DD	Translational norm (m)	3.3043×10^{-2}	0.423	4.5989	0.421	9.9393×10^{-8} m
VCL-IS	Rotational norm (rad)	3.2314×10^{-1}	0.482	4.1932×10^{-5}	0.483	2.4895×10^{-6} rad
VCL-IS	Translational norm (m)	4.3253×10^{-2}	0.484	4.4648×10^{-5}	0.484	3.5180×10^{-7} m

matrices share the same rotation matrix $\boldsymbol{V}$ as the inertia matrix. Therefore, $\boldsymbol{D}_d$ and $\boldsymbol{K}_d$ can be expressed as follows:

$$\begin{aligned} \boldsymbol{D}_d &= \boldsymbol{V}\boldsymbol{\lambda}_D\boldsymbol{V}^T, \\ \boldsymbol{K}_d &= \boldsymbol{V}\boldsymbol{\lambda}_K\boldsymbol{V}^T. \end{aligned} \tag{12}$$

The eigenvalues of the decoupled inertia, damping, and stiffness matrices follow the parameter relationships of a second-order linear SISO system; specifically, the diagonal eigenvalue matrices of damping and stiffness satisfy the following empirical relationships:

$$\begin{aligned} \boldsymbol{\lambda}_D &= 2\zeta\kappa\boldsymbol{\lambda}_\Lambda\boldsymbol{\omega}, \\ \boldsymbol{\lambda}_K &= \kappa^2\boldsymbol{\lambda}_\Lambda\boldsymbol{\omega}^2, \\ \kappa &= \frac{1}{\sqrt{(1-2\zeta^2)+\sqrt{2-4\zeta^2+4\zeta^4}}}. \end{aligned} \tag{13}$$

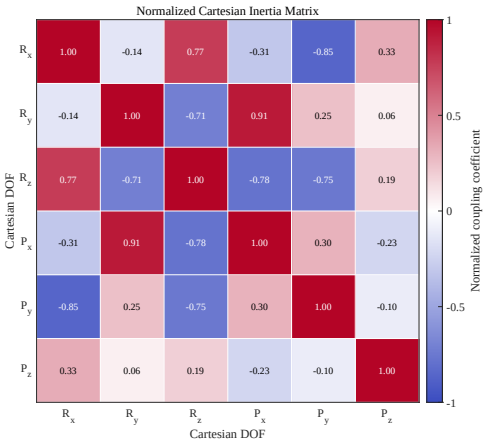


Fig. 3. Normalized six-dimensional Cartesian inertia matrix at the selected robot configuration. The off-diagonal entries indicate substantial coupling between rotational and translational degrees of freedom.

Here, $\boldsymbol{\lambda}_\Lambda$, $\boldsymbol{\lambda}_D$ and $\boldsymbol{\lambda}_K$ are the diagonal eigenvalue matrices of $\boldsymbol{\Lambda}_d$, $\boldsymbol{D}_d$, and $\boldsymbol{K}_d$, respectively; ζ is a scalar associated with the weighting ratio ρ, and $\boldsymbol{\omega}$ is the diagonal matrix of modal frequencies. These matrices are defined in the same modal basis, so the impedance matrices share a common modal orientation. The coupled impedance can therefore be interpreted in the inertia-related coordinate system, and the modal relationships among inertia, damping, and stiffness resemble those of a second-order SISO system.

The ellipsoids of inertia, damping, and stiffness for three coupled two-dimensional inertia matrices are illustrated in Fig. 5. The empirical statistics are consistent with (13): the eigenvalues of $\boldsymbol{D}_d$ and the square roots of the eigenvalues of $\boldsymbol{K}_d$ vary approximately linearly with the modal frequency ω_b, with fitted lines passing through the origin. In addition, because the setting of $\rho = 1$ is unchanged, the equivalent Cartesian modal damping-ratio curves remain close to a unit circle for the tested inertia matrices and bandwidth settings. This suggests that, when response, aggregate robustness, and stability are jointly considered, the optimized damping tends toward a near-critical-damping balance. The optimized six-dimensional impedance exhibits a similar trend.

V. Time-Varying VCL-IS Impedance Design

The Cartesian inertia of a robot varies with its pose. If the desired inertia is selected to match the actual Cartesian inertia at each instant, i.e., $\boldsymbol{\Lambda}_d(t) = \boldsymbol{\Lambda}(t)$, the damping and stiffness matrices must be updated accordingly. The empirical parameterization in (12) and (13) can be extended to time-varying inertia. Here, ζ is a user-selected constant, and the time-varying modal-frequency matrix is defined as $\boldsymbol{\omega}(t) = \mathrm{diag}(\omega_1(t), \omega_2(t), \ldots, \omega_n(t))$. However, stability analysis for a constant impedance cannot be directly applied to the time-varying case. The distribution of the time-varying modal frequencies must be constrained, while their task-dependent adaptation law can be learned.

A. Stability Constraint for Time-Varying VCL-IS Impedance

A common quadratic Lyapunov function is used to derive a sufficient admissible range for the time-varying modal frequencies. Substituting the time-varying parameterization into (1) gives the following impedance-response error model:

$$\ddot{\boldsymbol{e}}(t) + 2\zeta \boldsymbol{S}(t)\dot{\boldsymbol{e}}(t) + \boldsymbol{S}^2(t)\boldsymbol{e}(t) = \boldsymbol{0},$$
$$\boldsymbol{S}(t) = \kappa \boldsymbol{V}(t)\boldsymbol{\omega}(t)\boldsymbol{V}^T(t).$$

For the illustrative case $\zeta = 1$, the error model becomes

$$\ddot{\boldsymbol{e}}(t) + 2\boldsymbol{S}(t)\dot{\boldsymbol{e}}(t) + \boldsymbol{S}^2(t)\boldsymbol{e}(t) = \boldsymbol{0}.$$

For any $\epsilon > 0$, let $s = \kappa\epsilon$. The Lyapunov function for the time-varying impedance is selected as follows:

$$V_L(\boldsymbol{x}) = \boldsymbol{x}^T(t)\boldsymbol{P}\boldsymbol{x}(t),$$
$$\boldsymbol{x}(t) = \begin{bmatrix} \boldsymbol{e}(t) \\ s^{-1}\dot{\boldsymbol{e}}(t) \end{bmatrix},$$
$$\boldsymbol{P} = \begin{bmatrix} 3\boldsymbol{I} & \boldsymbol{I} \\ \boldsymbol{I} & \boldsymbol{I} \end{bmatrix} \succ 0.$$

Clearly, $\boldsymbol{P} \succ 0$. A sufficient condition for stability is that the state matrix satisfy the following Lyapunov equation for a constant positive-definite matrix $\boldsymbol{P}$:

$$\boldsymbol{A}_v^T(t)\boldsymbol{P} + \boldsymbol{P}\boldsymbol{A}_v(t) = -\boldsymbol{Q}, \qquad \boldsymbol{Q} \succ 0.$$

Here, $\boldsymbol{A}_v(t)$ is the state matrix of the error model, and $\boldsymbol{P}$ is the constant matrix defined above. Applying the Schur-complement condition yields the following sufficient modal-frequency interval:

$$0.7325\epsilon < \omega_i(t) < 4.0960\epsilon.$$

The lower bound is $\omega_{\min} = 0.7325\epsilon$, and the upper bound satisfies $\omega_{\max} < 5.5918\omega_{\min}$. This result is a sufficient stability bound derived for equal weighting of compliance and aggregate robustness and for the specified Lyapunov matrix $\boldsymbol{P}$; it is not a necessary condition for all time-varying impedance designs. In implementation, the policy output should be constrained to the admissible interval at every time step. If the impedance weights or $\boldsymbol{P}$ change, the sufficient bound should be recomputed.

B. SAC-Based Time-Varying Impedance Adaptation

The time-varying impedance adaptation policy is modeled using SAC as $\boldsymbol{\omega}(t) = \pi_\theta(\boldsymbol{\Lambda}(t), \omega_b)$. Under the inertia-matching condition $\boldsymbol{\Lambda}_d(t) = \boldsymbol{\Lambda}(t)$, its inputs are $\boldsymbol{\Lambda}_d(t)$ and ω_b, and its output is $\boldsymbol{\omega}(t)$. The diagonal entries of $\boldsymbol{\omega}(t)$ are constrained to the admissible interval $\omega_{\min} < \omega_i(t) < \omega_{\max}$ obtained from the Lyapunov analysis. Given the policy output, the structured VCL-IS relationships in (12) and (13) are used to construct $\boldsymbol{D}_d(t)$ and $\boldsymbol{K}_d(t)$, and the instantaneous impedance loss $L(t)$ is evaluated. The SAC objective is to minimize $L(t)$.

The SAC-based time-varying impedance policy is evaluated in a seven-axis robot simulation to assess the extension of VCL-IS to time-varying systems. FAC and DD are used as comparison methods. dDCI and DCI are excluded because of their insufficient stability in the tested complex time-varying

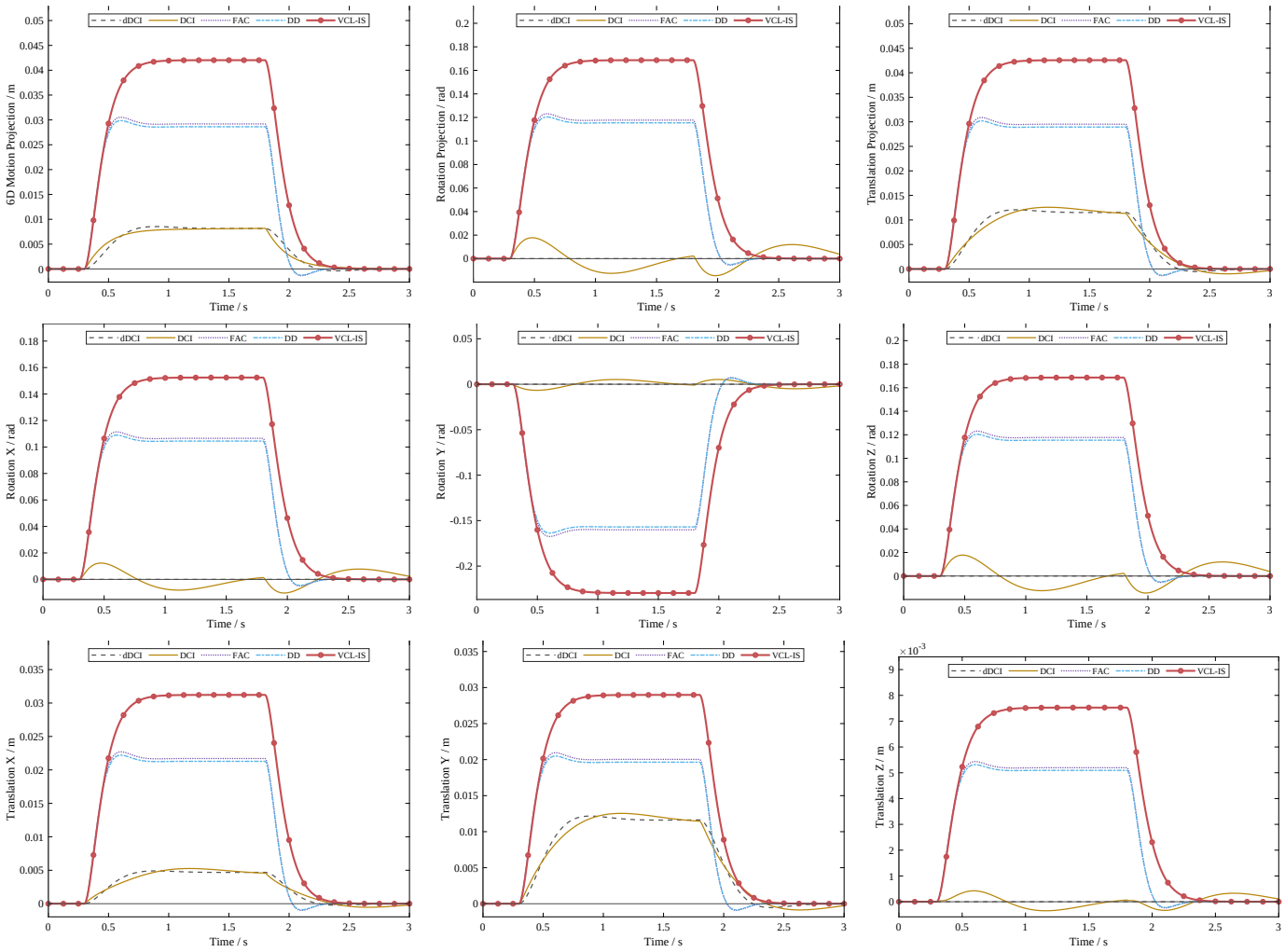


Fig. 4. Six-dimensional response comparison under a strongly coupled Cartesian inertia matrix. The first row shows the overall motion indicator, the second row shows rotational-axis responses, and the third row shows translational-axis responses.

system. All three compared methods are implemented using the same classical impedance controller. The results are shown in Fig. 7.

The simulation supports the feasibility of extending VCL-IS from fixed-inertia matrices to time-varying inertia systems. Compared with FAC and DD, VCL-IS maintains larger compliant displacements while suppressing overshoot. The time-varying results therefore retain the main performance characteristics observed in the constant-impedance simulations.

VI. Robot Experiments

Physical robot experiments are conducted to evaluate the aggregate robustness of the impedance realization. In practice, the commanded and actual contact forces differ, feedback signals contain noise, and model parameters are imperfect. The ability of a controller to keep the measured response close to the theoretical impedance response therefore provides an empirical test of aggregate realization robustness.

A. Experimental Setup

A seven-degree-of-freedom Franka Emika Panda robot is used. Different impedance-design methods are compared using the same classical Cartesian impedance controller. A linear motor applies a thrust to the robot end effector through a thrust plane. A contact-force sensor is installed behind the thrust plate to close the loop on the commanded contact force. A universal ball bearing is mounted at the robot end effector and contacts the thrust disk driven by the linear motor, forming a spherical pair. This interface constrains the contact-force direction to align with the linear-motor axis and reduces parasitic coupling between robot motion and the environment. The experimental setup is shown in Fig. 8.

B. Experimental Procedure and Reference Response

FAC, DD, and VCL-IS use the same classical impedance controller; only the impedance-parameter design method differs. VCL-IS uses the same policy π_θ as in the simulation. The experimental input consists of a two-variable step response in $\boldsymbol{F}_{\text{ext}}$ and ω_b. The contact force is increased from a low preload to approximately 25 N at $t = 1$ s. The preload prevents a gap and reduces impact at contact. The target bandwidth follows a three-level sequence: 6 rad/s from 0 to 4 s, 8 rad/s from 4 to 7 s, and 10 rad/s from 7 to 10 s. This experiment examines the effects of both an external contact-force step and changes in the

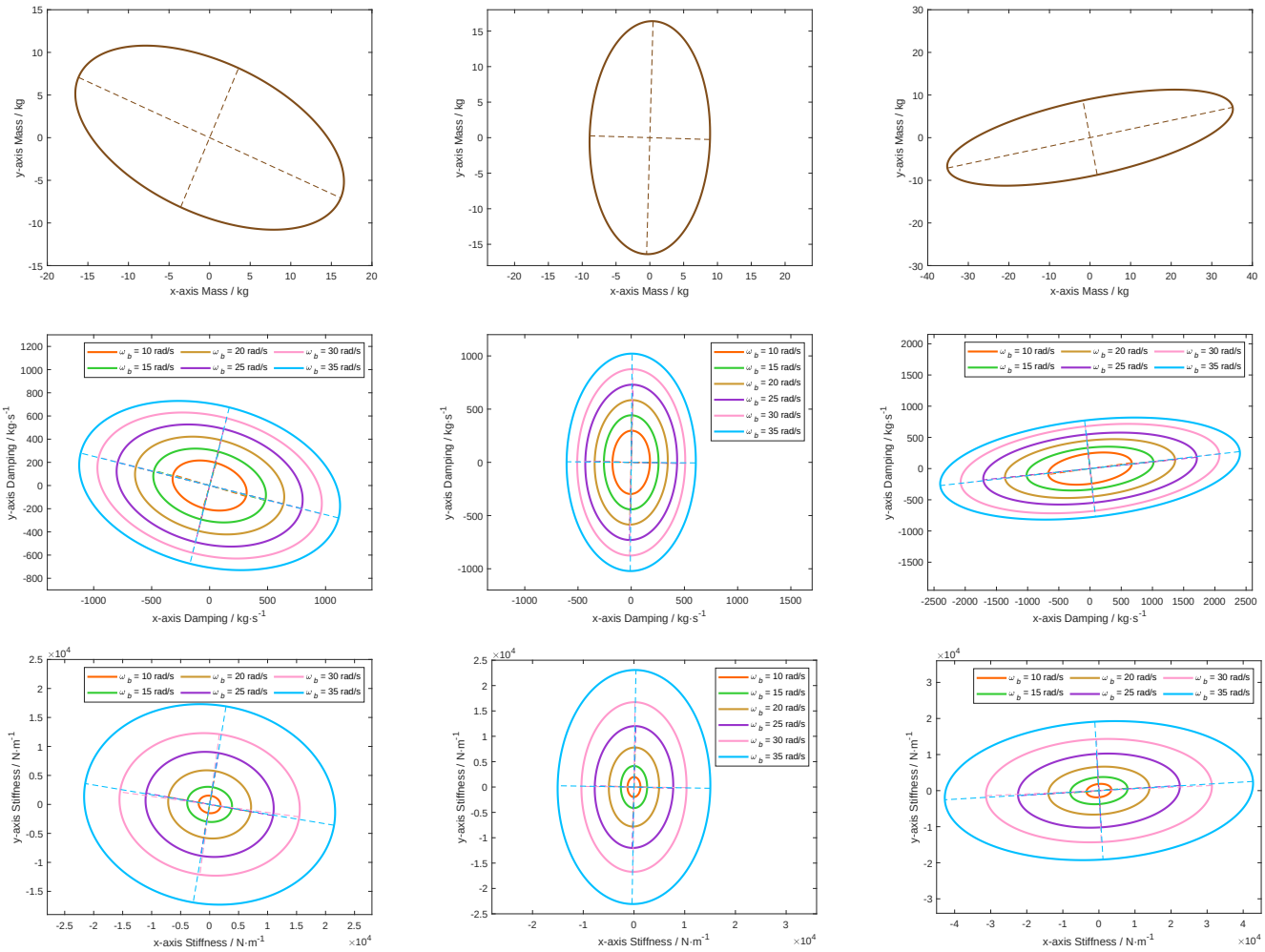


Fig. 5. Inertia, damping, and stiffness ellipsoids for three coupled two-dimensional inertia matrices. From top to bottom, the rows show the inertia, damping, and stiffness ellipsoids, respectively; the columns correspond to the three inertia matrices. The damping and stiffness ellipsoids are plotted for different target bandwidths ω_b.

internal performance-design parameter. The measured contact force and target-bandwidth sequence are shown in Fig. 9.

For each impedance-design method, the theoretical impedance response is compared with the measured robot response. The comparison includes the six-dimensional motion norm, rotational and translational norms, and each Cartesian component. The discrepancy between the theoretical and measured responses is used as an aggregate-robustness indicator, reflecting the combined effects of unmodeled dynamics, sensor noise, disturbances, and parameter mismatch. The response comparisons are shown in Fig. 10.

C. Aggregate-Robustness Evaluation

The same six-dimensional displacement measure introduced in Section IV-B is used to evaluate the discrepancy between the measured and theoretical responses. The normalized discrepancies are calculated over the experimental samples. During the contact-force step and target-bandwidth transitions, VCL-IS exhibits a substantially smaller weighted six-dimensional response discrepancy than the other methods. The normalized response discrepancies for FAC, DD, and VCL-IS are 17.0817%, 16.5843%, and 2.1475%, respectively. Relative to FAC and DD, the discrepancy obtained with VCL-IS is reduced by approximately 87.4% and 87.0%, respectively. The aggregate comparison is shown in Fig. 11.

The axis-wise statistics and six-dimensional aggregate metrics are listed in Table II. VCL-IS reduces the normalized discrepancy in all six Cartesian directions. Its largest remaining discrepancy occurs along P_z and is 11.49%; the discrepancies in the other five components are all below 1%.

These results indicate that, under the tested operating conditions, VCL-IS provides better aggregate robustness: despite the contact-force step and target-bandwidth changes, the measured response remains closer to the theoretical impedance response. The experiment does not separate disturbance rejection from parameter-uncertainty effects, because both occur together with other implementation errors. The reported result should therefore be interpreted as aggregate robustness rather than as evidence for independently quantified robustness mechanisms.

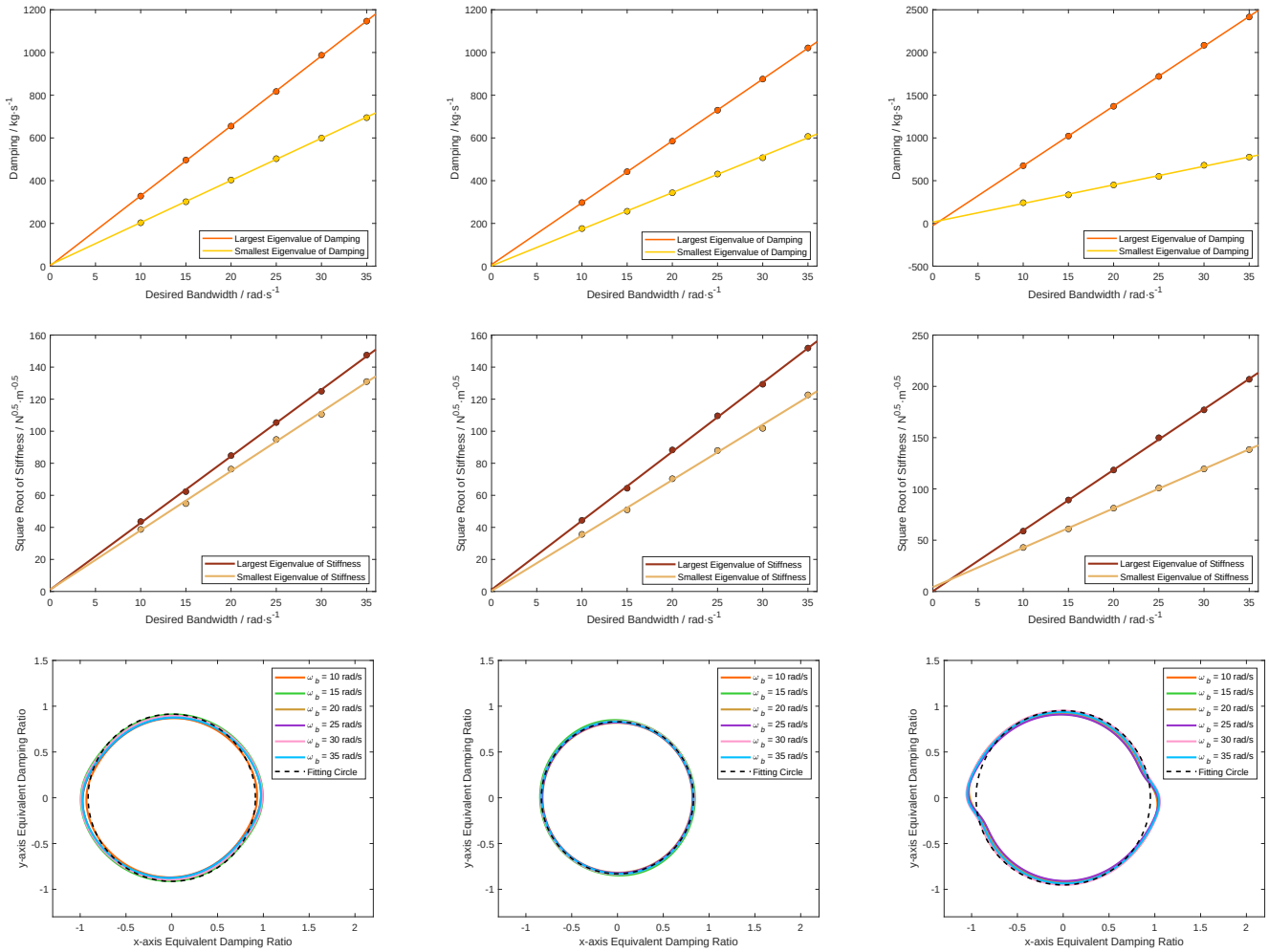


Fig. 6. Modal trends for three coupled two-dimensional inertia matrices. From top to bottom, the rows show the damping eigenvalues, square roots of the stiffness eigenvalues, and equivalent modal damping ratios, respectively; the columns correspond to the three inertia matrices. The curves show the dependence on the target bandwidth ω_b.

VII. Discussion

The numerical simulations and physical experiments support the design motivation of VCL-IS. First, the virtual contact loop provides explicit performance channels for compliance and aggregate robustness. The weighted generalized-plant $\mathcal{H}_2/\mathcal{H}_\infty$ norms quantify energy-related and worst-case input–output gains, while α discourages slow or unstable impedance dynamics. Second, the simulation results indicate that higher compliance does not necessarily require simply reducing damping and accepting oscillatory behavior. Under the reported conditions, VCL-IS generally produces larger displacements than FAC/DD while maintaining low overshoot. Third, the physical robot experiment shows that VCL-IS is less sensitive to the tested target-bandwidth changes in terms of the discrepancy between theoretical and measured responses.

Several limitations should be acknowledged. Although the loss function L is not unique, the formulation adopted in this paper provides an effective way to balance the two objectives. Ablation studies show that optimizing solely to minimize γ causes the optimization process to converge very slowly, whereas maximizing α alone drives the desired stiffness toward infinity. These findings support the effectiveness of the proposed formulation but do not establish its optimality. The hyperparameters ω_b and ω_c can substantially affect the dynamic response of the impedance, including settling time and bandwidth; however, their effects cannot yet be characterized precisely and quantitatively. A notable advantage of VCL-IS is that its response to changes in the internal parameter ω_b is stable and smooth. This behavior suggests potential for task-oriented adaptive impedance control. Nevertheless, using ω_b to realize task-oriented variable-impedance adaptation requires further investigation.

VIII. Conclusion

This paper proposed VCL-IS, a performance-oriented Cartesian impedance synthesis method based on a virtual contact loop. The method transforms the synthesis of a strongly coupled MIMO impedance into a weighted performance-optimization problem for a virtual closed-loop system. By combining the weighted $\mathcal{H}_2/\mathcal{H}_\infty$ performance of the generalized plant with the negative spectral abscissa α, the proposed objective balances compliance, asymptotic convergence, and

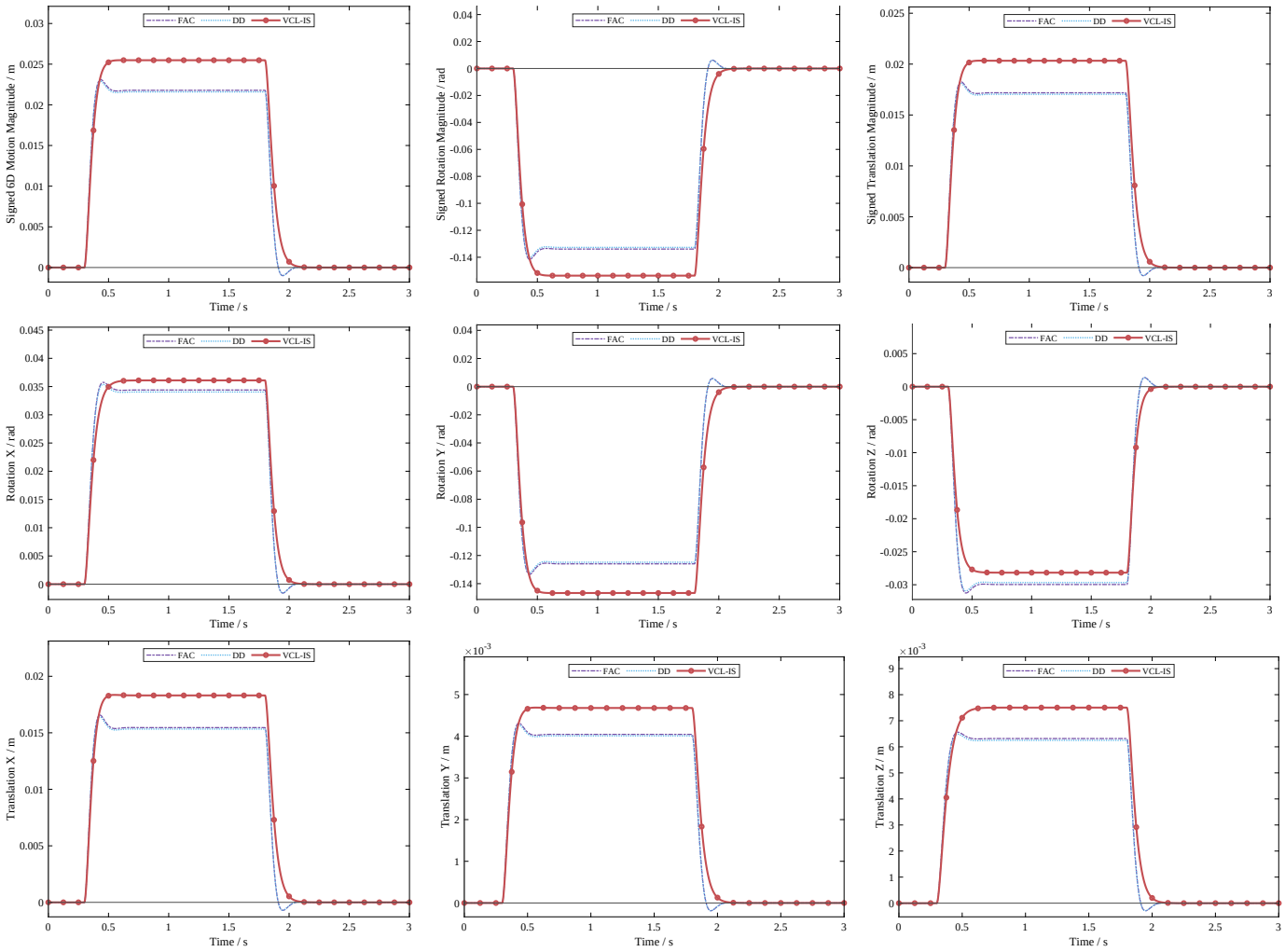


Fig. 7. Time-varying impedance simulation comparing FAC, DD, and VCL-IS. The overall motion indicator and six Cartesian components indicate that, under the tested time-varying conditions, VCL-IS achieves larger compliant motion while maintaining very small overshoot.

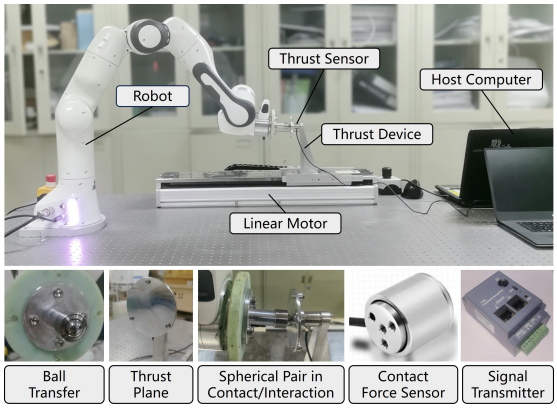


Fig. 8. Experimental setup. The Franka Emika Panda robot interacts with the linear-motor thrust device through a spherical contact interface. The force sensor and motor feedback controller regulate the contact-force magnitude, while the spherical pair constrains the force direction.

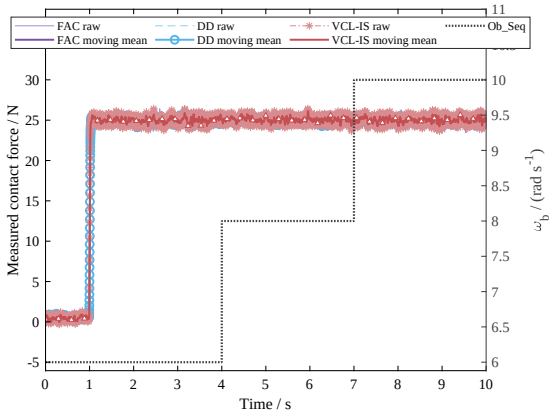


Fig. 9. Measured contact force and target-bandwidth schedule in the robot experiment. The contact force steps at 1 s, while the target bandwidth changes at 4 and 7 s.

aggregate robustness. Numerical analysis revealed an interpretable structure in the optimized impedance matrices: $\boldsymbol{\Lambda}_d(t)$, $\boldsymbol{D}_d(t)$, and $\boldsymbol{K}_d(t)$ share a common modal basis and are geometrically decoupled through their modal transformation. For time-varying impedance, a common quadratic Lyapunov analysis yielded a sufficient admissible range for the modal-frequency matrix $\boldsymbol{\omega}(t)$, which was imposed on an SAC-based adaptation policy.

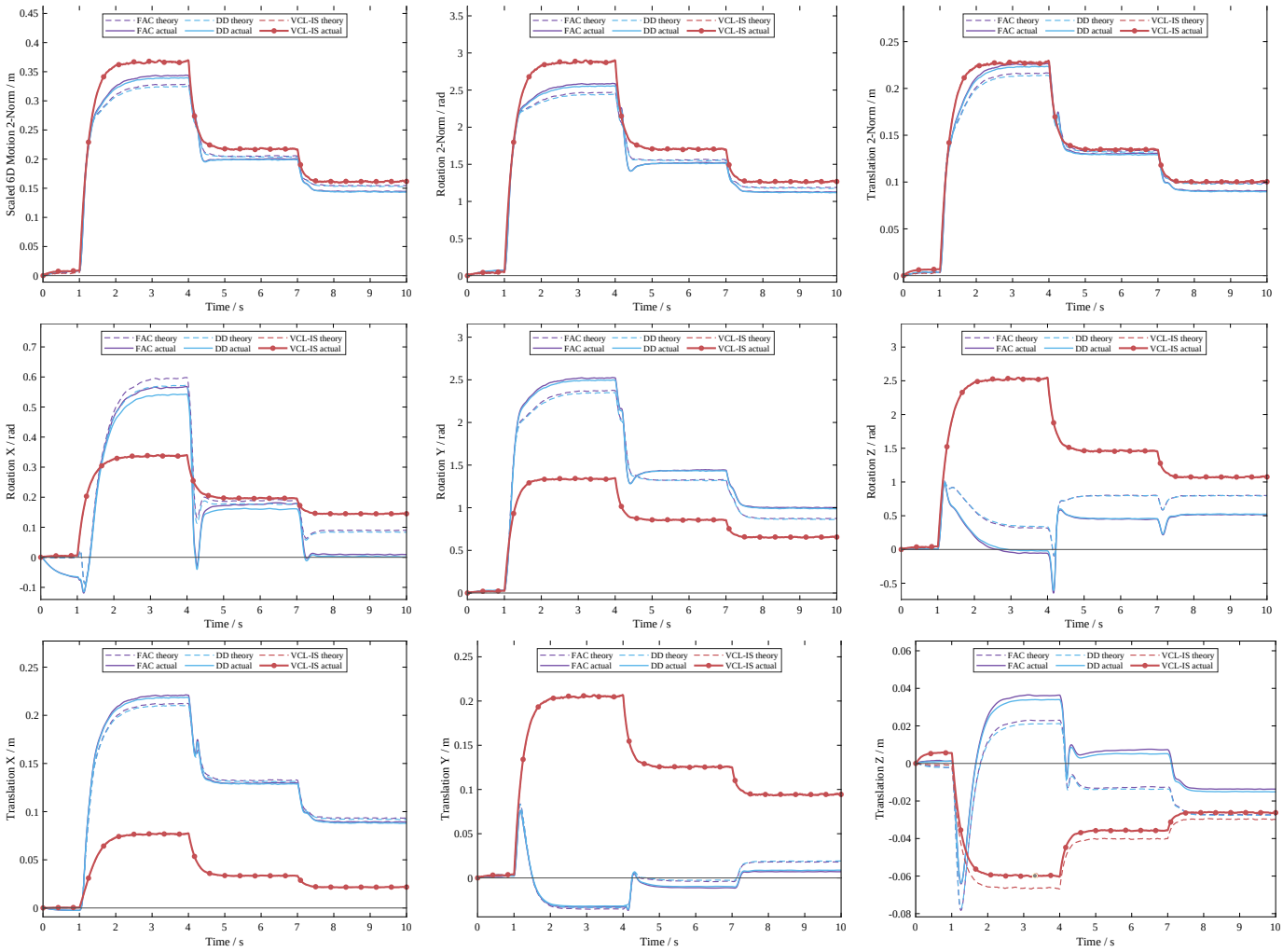
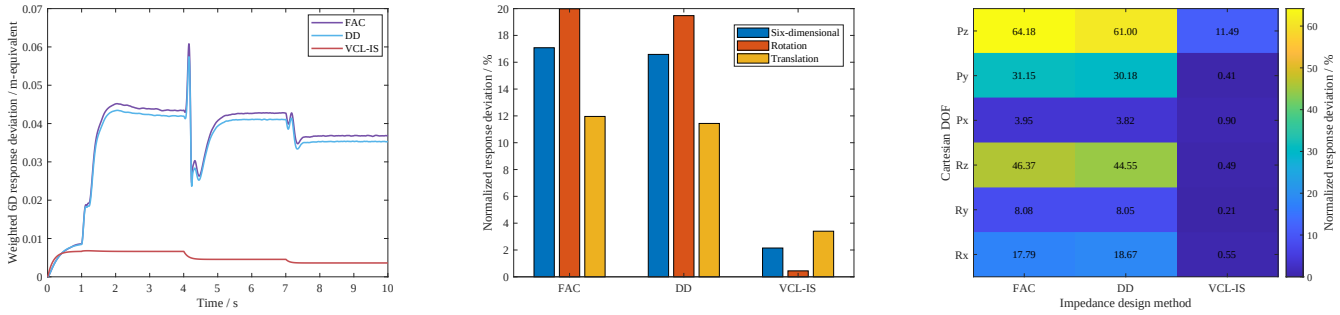


Fig. 10. Comparison of theoretical and measured responses for FAC, DD, and VCL-IS in the robot experiment. The subplots show the six-dimensional motion norm, rotational and translational norms, and the six Cartesian components.



(a) (b) (c)

Fig. 11. Aggregate response-discrepancy evaluation: (a) weighted six-dimensional response deviation over time; (b) normalized discrepancies of the six-dimensional, rotational, and translational responses; and (c) normalized discrepancies for the six Cartesian degrees of freedom.

The two- and six-dimensional simulations showed that VCL-IS can exploit system coupling to obtain larger compliant responses with low overshoot at comparable response speeds. In the Franka Emika Panda experiment, the normalized discrepancy between theoretical and measured six-dimensional responses was 2.1475%, substantially lower than the 17.0817% and 16.5843% obtained with FAC and DD. These results suggest that VCL-IS provides a promising approach to synthesizing coupled Cartesian impedance from task-level interaction objectives. Future work will investigate quantitative performance shaping and task-oriented adaptive variable-impedance control.

Acknowledgment

This work was supported by the National Natural Science Foundation of China under Grant 52175029.

TABLE II
AXIS-WISE AND SIX-DIMENSIONAL RESPONSE-DISCREPANCY STATISTICS BETWEEN THEORETICAL AND MEASURED ROBOT RESPONSES.

Method	DOF	Unit	RMSE	NRMSE (%)	Maximum absolute error
FAC	R_x	rad	0.053523	17.791	0.16679
	R_y	rad	0.12262	8.078	0.19572
	R_z	rad	0.30909	46.366	0.57575
	P_x	m	0.005516	3.9466	0.012328
	P_y	m	0.0070384	31.151	0.01097
	P_z	m	0.014634	64.181	0.019958
	6D	m-equivalent	0.037795	17.0817	0.060801
DD	R_x	rad	0.053647	18.666	0.15839
	R_y	rad	0.121	8.0451	0.18252
	R_z	rad	0.29712	44.551	0.54249
	P_x	m	0.0052809	3.8157	0.011896
	P_y	m	0.0067057	30.179	0.010388
	P_z	m	0.013815	61.005	0.01883
	6D	m-equivalent	0.036355	16.5843	0.057427
VCL-IS	R_x	rad	0.0011981	0.5454	0.0026354
	R_y	rad	0.0019462	0.21161	0.003283
	R_z	rad	0.0080934	0.49243	0.012436
	P_x	m	0.00039862	0.89694	0.00066327
	P_y	m	0.00056091	0.4083	0.00086624
	P_z	m	0.0050911	11.493	0.0067233
	6D	m-equivalent	0.0052058	2.1475	0.0068051

6D denotes the length-equivalent displacement measure defined in Section IV-B.

REFERENCES

[1] N. Hogan, "Impedance control: An approach to manipulation—Part I: Theory," *Journal of Dynamic Systems, Measurement, and Control*, vol. 107, no. 1, pp. 1–7, 1985, doi: 10.1115/1.3140702.

[2] J. K. Salisbury, "Active stiffness control of a manipulator in Cartesian coordinates," in *Proc. 19th IEEE Conf. Decision and Control*, Albuquerque, NM, USA, 1980, pp. 95–100, doi: 10.1109/CDC.1980.272026.

[3] M. H. Raibert and J. J. Craig, "Hybrid position/force control of manipulators," *Journal of Dynamic Systems, Measurement, and Control*, vol. 103, no. 2, pp. 126–133, 1981, doi: 10.1115/1.3139652.

[4] O. Khatib, "A unified approach for motion and force control of robot manipulators: The operational space formulation," *IEEE Journal on Robotics and Automation*, vol. 3, no. 1, pp. 43–53, 1987, doi: 10.1109/JRA.1987.1087068.

[5] O. Khatib, "Inertial properties in robotic manipulation: An object-level framework," *The International Journal of Robotics Research*, vol. 14, no. 1, pp. 19–36, 1995, doi: 10.1177/027836499501400103.

[6] A. Albu-Schäffer, C. Ott, U. Frese, and G. Hirzinger, "Cartesian impedance control of redundant robots: Recent results with the DLR-light-weight-arms," in *Proc. IEEE Int. Conf. Robotics and Automation*, 2003, vol. 3, pp. 3704–3709, doi: 10.1109/ROBOT.2003.1242165.

[7] C. Ott, A. Albu-Schäffer, A. Kugi, and G. Hirzinger, "Decoupling based Cartesian impedance control of flexible joint robots," in *Proc. IEEE Int. Conf. Robotics and Automation*, 2003, vol. 3, pp. 3101–3107, doi: 10.1109/ROBOT.2003.1242067.

[8] K. Kronander and A. Billard, "Stability considerations for variable impedance control," *IEEE Transactions on Robotics*, vol. 32, no. 5, pp. 1298–1305, 2016, doi: 10.1109/TRO.2016.2593492.

[9] F. J. Abu-Dakka and M. Saveriano, "Variable impedance control and learning—A review," *Frontiers in Robotics and AI*, vol. 7, Art. no. 590681, 2020, doi: 10.3389/frobt.2020.590681.

[10] T. Sun, L. Peng, L. Cheng, Z.-G. Hou, and Y. Pan, "Stability-guaranteed variable impedance control of robots based on approximate dynamic inversion," *IEEE Transactions on Systems, Man, and Cybernetics: Systems*, vol. 51, no. 7, pp. 4193–4200, 2021, doi: 10.1109/TSMC.2019.2930582.

[11] Y. Michel, C. Ott, and D. Lee, "Passivity-based variable impedance control for redundant manipulators," *IFAC-PapersOnLine*, vol. 53, no. 2, pp. 9865–9872, 2020, doi: 10.1016/j.ifacol.2020.12.2692.

[12] Y. Michel, C. Ott, and D. Lee, "Safety-aware hierarchical passivity-based variable compliance control for redundant manipulators," *IEEE Transactions on Robotics*, vol. 38, no. 6, pp. 3899–3916, 2022, doi: 10.1109/TRO.2022.3174478.

[13] X. Zhang, L. Sun, Z. Kuang, and M. Tomizuka, "Learning variable impedance control via inverse reinforcement learning for force-related tasks," *IEEE Robotics and Automation Letters*, vol. 6, no. 2, pp. 2225–2232, 2021, doi: 10.1109/LRA.2021.3061374.

[14] S. A. Khader, H. Yin, P. Falco, and D. Kragic, "Stability-guaranteed reinforcement learning for contact-rich manipulation," *IEEE Robotics and Automation Letters*, vol. 6, no. 1, pp. 1–8, 2021, doi: 10.1109/LRA.2020.3028529.

[15] H. Zhang, G. Solak, G. J. G. Lahr, and A. Ajoudani, "SRL-VIC: A variable stiffness-based safe reinforcement learning for contact-rich robotic tasks," *IEEE Robotics and Automation Letters*, vol. 9, no. 6, pp. 5631–5638, 2024, doi: 10.1109/LRA.2024.3396368.

[16] H. Wu, Q. Hu, J. Zheng, X. Shao, Y. Liu, and D. Li, "Reinforcement learning for robot optimal impedance control: Theoretical feasibility and extensibility analysis," *IEEE Transactions on Industrial Electronics*, vol. 73, no. 3, pp. 4251–4261, 2026, doi: 10.1109/TIE.2025.3607988.

[17] R. S. Sutton and A. G. Barto, *Reinforcement Learning: An Introduction*, 2nd ed. Cambridge, MA, USA: MIT Press, 2018.

[18] T. Haarnoja, A. Zhou, P. Abbeel, and S. Levine, "Soft actor-critic: Off-policy maximum entropy deep reinforcement learning with a stochastic actor," in *Proc. 35th Int. Conf. Machine Learning*, PMLR, vol. 80, 2018, pp. 1861–1870.

[19] A. Albu-Schäffer, C. Ott, and G. Hirzinger, "A unified passivity-based control framework for position, torque and impedance control of flexible joint robots," *The International Journal of Robotics Research*, vol. 26, no. 1, pp. 23–39, 2007, doi: 10.1177/0278364907073776.

[20] J. E. Colgate and N. Hogan, "Robust control of dynamically interacting systems," *International Journal of Control*, vol. 48, no. 1, pp. 65–88, 1988, doi: 10.1080/00207178808906161.

[21] C. Saldarriaga, N. Chakraborty, and I. Kao, "Damping selection for Cartesian impedance control with dynamic response modulation," *IEEE Transactions on Robotics*, vol. 38, no. 3, pp. 1915–1924, 2022, doi: 10.1109/TRO.2021.3116855.

[22] Y. Huang, S. Li, and Q. Huang, "Robust impedance control for SEAs," *Journal of the Franklin Institute*, vol. 357, no. 12, pp. 7921–7943, 2020, doi: 10.1016/j.jfranklin.2020.06.015.

[23] Y. C. Huang and N. F. Shao, "LMI-based impedance control synthesis: A case study on fixed-stiffness actuators (FSAs)," *International Journal of Control*, vol. 96, no. 12, pp. 2945–2957, 2023, doi: 10.1080/00207179.2022.2119433.

[24] D. Larby and F. Forni, "A passivity preserving H_∞ synthesis technique for robot control," in *Proc. IEEE 61st Conf. Decision and Control*, 2022, pp. 1416–1422, doi: 10.1109/CDC51059.2022.9993347.

[25] N. Shao and Y. Huang, "Frequency-shaped μ-synthesis with force-guided reference shaping for robust impedance control of robots," *Robotics and Autonomous Systems*, vol. 204, Art. no. 105534, 2026, doi: 10.1016/j.robot.2026.105534.

[26] S. Skogestad and I. Postlethwaite, *Multivariable Feedback Control: Analysis and Design*, 2nd ed. Chichester, U.K.: Wiley, 2005.

[27] J. C. Doyle, K. Glover, P. P. Khargonekar, and B. A. Francis, "State-space solutions to standard H_2 and H_∞ control problems," *IEEE Transactions on Automatic Control*, vol. 34, no. 8, pp. 831–847, 1989, doi: 10.1109/9.29425.

[28] S. Boyd, L. El Ghaoui, E. Feron, and V. Balakrishnan, *Linear Matrix Inequalities in System and Control Theory*. Philadelphia, PA, USA: SIAM, 1994.

[29] J. V. Burke, A. S. Lewis, and M. L. Overton, "Optimization and pseudospectra, with applications to robust stability," *SIAM Journal on Matrix Analysis and Applications*, vol. 25, no. 1, pp. 80–104, 2003, doi: 10.1137/S0895479802402818.

[30] H. K. Khalil, *Nonlinear Systems*, 3rd ed. Upper Saddle River, NJ, USA: Prentice Hall, 2002.

[31] F. Ferraguti, C. Secchi, and C. Fantuzzi, "A tank-based approach to impedance control with variable stiffness," in *Proc. IEEE Int. Conf. Robotics and Automation*, 2013, pp. 4948–4953, doi: 10.1109/ICRA.2013.6631284.

[32] G. Raiola, C. A. Cardenas, T. S. Tadele, T. de Vries, and S. Stramigioli, "Development of a safety- and energy-aware impedance controller for collaborative robots," *IEEE Robotics and Automation Letters*, vol. 3, no. 2, pp. 1237–1244, 2018, doi: 10.1109/LRA.2018.2795639.

[33] J. Lachner, F. Allmendinger, S. Stramigioli, and N. Hogan, "Shaping impedances to comply with constrained task dynamics," *IEEE Transactions on Robotics*, vol. 38, no. 5, pp. 2750–2767, Oct. 2022, doi: 10.1109/TRO.2022.3153949.

[34] Z. Zhou, X. Yang, and X. Zhang, "Variable impedance control on contact-rich manipulation of a collaborative industrial mobile manipulator: An imitation learning approach," *Robotics and Computer-Integrated Manufacturing*, vol. 92, Art. no. 102896, Apr. 2025, doi: 10.1016/j.rcim.2024.102896.

[35] X. Tang, J. Yang, and H. Ding, "Design and control of a parallel electromagnetic variable stiffness manipulator for robotic compliant grinding," *Robotics and Computer-Integrated Manufacturing*, vol. 98, Art. no. 103158, Apr. 2026, doi: 10.1016/j.rcim.2025.103158.